MIT Open Access Articles

Ghost imaging in reflection: Resolution, contrast, and signal-to-noise ratio

Massachusetts Institute of Technology

DSpace@MIT

Ghost Imaging in Reflection: Resolution, Contrast, and Signal-to-Noise Ratio

Nicholas D. Hardy and Jeffrey H. Shapiro

Research Laboratory of Electronics
Massachusetts Institute of Technology,
Cambridge MA 02139

ABSTRACT

Ghost imaging is a transverse imaging technique that relies on the correlation between a pair of light fields, one that has interacted with the object to be imaged and one that has not. Most ghost imaging experiments have been performed in transmission, and virtually all ghost imaging theory has addressed the transmissive case. Yet stand-off sensing applications require that the object be imaged in reflection. We use Gaussian-state analysis to develop expressions for the spatial resolution, image contrast, and signal-to-noise ratio for reflective ghost imaging with a pseudothermal light source and a rough-surfaced object that creates target-returns with fully-developed speckle. We compare our results to the corresponding behavior seen in transmissive ghost imaging, and we develop performance results for the reflective form of computational ghost imaging. We also provide a preliminary stand-off sensing performance comparison between reflective ghost imaging and a conventional direct-detection laser radar.

Keywords: Ghost imaging, spatial resolution, image contrast, signal-to-noise ratio, laser radar

1. INTRODUCTION

Ghost imaging exploits the correlation between two light fields to create an image that neither field alone could provide. In pseudothermal ghost imaging—the primary case we shall consider—a continuous-wave (cw) laser beam is rendered spatially incoherent by passage through a rotating ground-glass diffuser, after which it is divided into signal and reference beams by a 50-50 beam splitter. The signal beam does not interact with the object of interest; after free-space propagation its transverse power distribution is measured using a high-spatial-resolution detector. The reference beam interacts with the object after free-space propagation and is then measured by a single-pixel (bucket) detector.[1,2] It follows that neither detector output alone suffices to produce an image; the bucket detector has no spatial resolution and the high-spatial-resolution detector senses light that has not interrogated the object. Cross correlating the photocurrents from the two detectors yields the ghost image, whose physical origin lies in the perfect correlation between the spatial fluctuations imposed by the rotating ground glass on the signal and reference beams. The first ghost imaging experiment was performed using biphotons obtained by post-selection from spontaneous parametric downconversion.[3] Because biphotons are entangled states, for which the quantum theory of photodetection is needed to calculate the measurement statistics, it was initially thought that ghost imaging was a quantum phenomenon. Gaussian-state analysis, however, has enabled a unified treatment of biphoton and pseudothermal ghost imaging that shows the image formation process is one of classical coherence propagation, with high contrast in DC-coupled biphoton ghost images being the principal ghost-image signature of that nonclassical source.[4] In particular, identical statistics for pseudothermal ghost-imaging result from the use of quantum photodetection theory, in which the light beams are treated quantum mechanically and photodetectors perform a quantum measurement, and semiclassical photodetection theory, in which the light beams are treated classically but photodetectors inject shot noise on top of any fluctuations in the illumination. For a thorough review of these considerations, see the recent paper by Erkmen and Shapiro.[5] For our purposes, it suffices to note that we can—and we will—use semiclassical photodetection theory in all that follows.

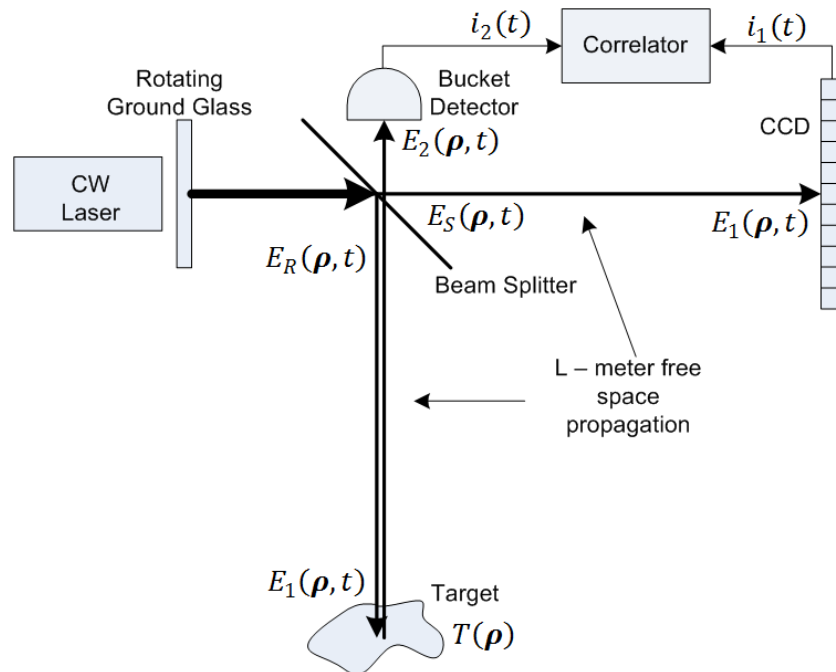Send correspondence to N. D. Hardy, e-mail: nhardy@mit.edu

Figure 1. Setup for pseudothermal reflective ghost imaging.

To date, Gaussian-state analysis of transmissive pseudothermal ghost imaging has provided expressions for its spatial resolution, image contrast and signal-to-noise ratio behaviors, i.e., a complete characterization of its performance.[4,6] However, one of the more interesting potential applications of ghost imaging is stand-off sensing, in which the bucket detector observes the object in reflection, not transmission. Preliminary table-top experiments have demonstrated the feasibility of this approach,[7] but there has been little exploration of the statistical characteristics of these images. Developing that theory within the Gaussian-state framework, which is the topic of this paper, must confront an additional complication not seen in previous work, viz., the speckle induced by reflection from rough-surfaced objects. In particular, we shall report expressions for the spatial resolution, image contract, and signal-to-noise ratio of pseudothermal reflective ghost imaging of speckle targets. These will be compared with the corresponding results for the transmissive case, in which there is no target-induced speckle. We will also use this framework to obtain performance results for the reflective form of computational ghost imaging,[8] in which the signal beam is dispensed with. Finally, we will provide a preliminary stand-off sensing performance comparison between reflective ghost imaging and a conventional direct-detection laser radar.

2. ANALYSIS OF PSEUDOTHERMAL REFLECTIVE GHOST IMAGING

2.1 Theoretical Setup

The configuration we shall consider for pseudothermal reflective ghost imaging is shown in Fig. 1. A cw laser beam is passed through a rotating ground-glass diffuser followed by a 50–50 beam splitter to produce identical, spatially-incoherent signal and reference beams whose temporal bandwidths are much lower than those of the single-pixel (bucket) and high-spatial-resolution (CCD array) detectors. The reference beam illuminates a rough-surfaced planar target at distance L from the beam splitter, and some of the light reflected from that target is collected, after L-m propagation, by the bucket detector. The signal light directly illuminates the CCD array, which for theoretical convenience, we have placed L-m away from the beam splitter.* The photocurrents from

---

*This assumption implies that we will form a 1:1 ghost image. In an actual implementation of reflective ghost imaging the CCD array would be in the focal plane of a lens located near the transmitter and we would obtain a minified ghost image.

the bucket detector and each pixel on the CCD are sent to a correlator, whose output for the CCD pixel located at transverse coordinate $\boldsymbol{\rho}_1$ is

$$C(\boldsymbol{\rho}_1) = \frac{1}{T_I} \int_{-T_I/2}^{T_I/2} dt\, i_1(t) i_2(t), \tag{1}$$

where T_I is the averaging time and we have suppressed an L/c time delay in $i_1(t)$ that is needed to account for the delay incurred by the light reflected from the target.

The configuration and notation we are using parallels the semiclassical treatment of transmissive ghost imaging,[8] with the principal distinction being that in the transmissive case the bucket detector would be behind a transmission-mask target L-m from the reference source, whereas here that target is viewed in reflection. Thus all the fields shown in Fig. 1 are complex envelopes about center frequency ω_0 of linearly-polarized light fields normalized to have $\sqrt{\text{photons/m}^2\text{s}}$ units as functions of their transverse coordinate vectors and time. As a result, under the assumption of shot-noise limited detectors with quantum efficiency η, the photocurrents from the bucket and the CCD can be written as

$$i_m(t) = \int d\tau\, [q\eta P_m(\tau) + \Delta i_m(\tau)]\, h(t-\tau), \quad \text{for } m = 1, 2. \tag{2}$$

Here: $P_m(t) = \int_{\mathcal{A}_m} d\boldsymbol{\rho}\, |E_m(\boldsymbol{\rho}, t)|^2$ is the photon flux on the circular active region $\mathcal{A}_m$ of detector m; q is the electron charge; $\Delta i_m(t)$ is the shot noise from detector m; and $h(t)$ is the detector's baseband impulse response, normalized to satisfy $\int dt\, h(t) = 1$. Physically, $q\eta P_m(t)$ is the conditional mean of $i_m(t)$, given the illumination, so that $\Delta i_m(t)$ is the photocurrent fluctuation conditioned on knowledge of the illumination. Note that given the photon-flux waveforms $\{P_m(t)\}$, the shot-noise currents $\Delta i_1(t)$ and $\Delta i_2(t)$ are statistically independent, zero-mean, random processes whose correlation functions are $\langle \Delta i_m(t_1) \Delta i_m(t_2) \rangle = q^2 \eta P_m(t_1) \delta(t_1 - t_2)$.

The fields that determine the preceding photon fluxes are found from diffraction theory. Given $E_S(\boldsymbol{\rho}, t)$, the signal field emerging from the beam splitter in Fig. 1, we have that the field illuminating the CCD is

$$E_1(\boldsymbol{\rho}, t) = \int d\boldsymbol{\rho}'\, E_S(\boldsymbol{\rho}', t) \frac{k_0 e^{ik_0(L + |\boldsymbol{\rho} - \boldsymbol{\rho}'|^2/2L)}}{i2\pi L}, \tag{3}$$

where $k_0 = \omega_0/c$ is the wave number at the center frequency ω_0, and we have neglected the L/c propagation delay. The reference field is identical to the signal field, because they are both obtained from 50-50 beam splitting of the output from the ground-glass diffuser. Thus this same $E_1(\boldsymbol{\rho}, t)$ illuminates the target in Fig. 1. After reflection from that target, the light arriving at the bucket detector is

$$E_2(\boldsymbol{\rho}, t) = \int d\boldsymbol{\rho}'\, E_1(\boldsymbol{\rho}', t) T(\boldsymbol{\rho}') \frac{k_0 e^{ik_0(L + |\boldsymbol{\rho} - \boldsymbol{\rho}'|^2/2L)}}{i2\pi L}, \tag{4}$$

where $T(\boldsymbol{\rho}')$ is the target's field-reflection coefficient,[†] and we have again neglected time delays. Whereas in transmissive ghost imaging it is ordinarily the case that the target's field-transmission coefficient is taken to be deterministic, the targets of interest for reflective ghost imaging will have microscopic surface variations—from a nominal, smooth surface profile—whose standard deviations can greatly exceed the illumination wavelength and whose transverse correlation scale can be sub-wavelength. When such a surface is illuminated by laser light it gives rise to laser speckle in the target return, and a reasonable statistical model for that behavior is to take $T(\boldsymbol{\rho}')$ to be a zero-mean, complex-valued, Gaussian random process that is completely characterized by the correlation function[9]

$$\langle T^*(\boldsymbol{\rho}_1') T(\boldsymbol{\rho}_2') \rangle = \lambda_0^2 \mathcal{T}(\boldsymbol{\rho}_1') \delta(\boldsymbol{\rho}_1' - \boldsymbol{\rho}_2'), \tag{5}$$

where λ_0 is the center wavelength of the illumination and $\mathcal{T}(\boldsymbol{\rho}')$ is the target's intensity-reflection coefficient, which is nonrandom and the quantity that we are seeking to image with the Fig. 1 setup.

At this point, we need to specify the source-field characteristics in order to proceed further. Following the Gaussian-state analysis of Erkmen and Shapiro,[4,6,8] we shall assume that $E_S(\boldsymbol{\rho}, t)$ and $E_R(\boldsymbol{\rho}, t)$—the identical

---

[†]We have assumed a stationary target, so that its field-reflection coefficient is constant in time.

outputs from the 50–50 beam splitter in Fig. 1—are zero-mean, complex-valued Gaussian random fields that are completely characterized by their common cross-spectrally pure phase-insensitive correlation function,

$$\langle E_S^*(\boldsymbol{\rho}_1, t_1) E_S(\boldsymbol{\rho}_2, t_2) \rangle = \langle E_R^*(\boldsymbol{\rho}_1, t_1) E_R(\boldsymbol{\rho}_2, t_2) \rangle = K(\boldsymbol{\rho}_1, \boldsymbol{\rho}_2) R(t_2 - t_1), \tag{6}$$

where

$$K(\boldsymbol{\rho}_1, \boldsymbol{\rho}_2) = \frac{2P}{\pi a_0^2} e^{-(|\boldsymbol{\rho}_1|^2 + |\boldsymbol{\rho}_2|^2)/a_0^2 - |\boldsymbol{\rho}_1 - \boldsymbol{\rho}_2|^2/2\rho_0^2} \tag{7}$$

is a Gaussian-Schell model spatial correlation with photon-flux P, e^{-2} intensity radius a_0, and coherence length ρ_0, and

$$R(t_2 - t_1) = e^{-(t_2 - t_1)^2/T_0^2} \tag{8}$$

is the normalized temporal correlation with correlation time T_0.

The preceding setup fully specifies all that is needed to compute the spatial resolution, image contrast, and signal-to-noise ratio of the pseudothermal reflective ghost image. Before doing so, however, let us introduce one final condition. We shall assume that the CCD pixel area, A_1, is sufficiently small that $|E_1(\boldsymbol{\rho}, t)|^2$ is essentially constant over each pixel, allowing us to use $P_1(t) = A_1 |E_1(\boldsymbol{\rho}, t)|^2$ in lieu of Eq. (2). This condition ensures that the spatial resolution we obtain is limited by the field statistics, not by the CCD's pixel size.

2.2 Spatial Resolution and Image Contrast

The spatial resolution and image contrast of the pseudothermal reflective ghost image are properties of the ensemble-averaged photocurrent cross correlation, i.e., Eq (1) averaged over the shot noise and the fluctuations in the fields that illuminate the two detectors. Those field fluctuations arise from the randomness imposed by the ground-glass diffuser and, for the field illuminating the bucket detector, the target's surface roughness. It is easy to see that the fields illuminating the detectors are zero-mean random processes that are statistically stationary in time, thus the ensemble-averaged ghost image satisfies

$$\langle C(\boldsymbol{\rho}_1) \rangle = \langle i_1(t) i_2(t) \rangle$$
$$= A_1 q^2 \eta^2 \int d\tau_1 \int d\tau_2 \int_{\mathcal{A}_2} d\boldsymbol{\rho}' \int d\boldsymbol{\rho}_2 \int d\boldsymbol{\rho}_3 \langle |E_1(\boldsymbol{\rho}_1, \tau_1)|^2 E_1^*(\boldsymbol{\rho}_2, \tau_2) E_1(\boldsymbol{\rho}_3, \tau_2) \rangle \langle T^*(\boldsymbol{\rho}_2) T(\boldsymbol{\rho}_3) \rangle$$
$$\times \frac{k_0 e^{-ik_0 |\boldsymbol{\rho}' - \boldsymbol{\rho}_2|^2/2L}}{-i2\pi L} \frac{k_0 e^{ik_0 |\boldsymbol{\rho}' - \boldsymbol{\rho}_3|^2/2L}}{i2\pi L} h(t - \tau_1) h(t - \tau_2), \tag{9}$$

where we have employed Eqs. (2) and (4), and exploited the statistical independence of $E_1(\boldsymbol{\rho}, t)$ and $T(\boldsymbol{\rho})$, i.e., the fluctuations due to propagation through the ground glass and those induced by the target's surface roughness. Making use of Eq. (5) then leads to

$$\langle C(\boldsymbol{\rho}_1) \rangle = \frac{A_1 A_2 q^2 \eta^2}{L^2} \int d\tau_1 \int d\tau_2 \int d\boldsymbol{\rho}_2 \langle |E_1(\boldsymbol{\rho}_1, \tau_1)|^2 |E_1(\boldsymbol{\rho}_2, \tau_2)|^2 \rangle \mathcal{T}(\boldsymbol{\rho}_2) h(t - \tau_1) h(t - \tau_2), \tag{10}$$

which clearly indicates the role of photon-flux correlation in ghost-image formation.

Equation (3) shows that $E_1(\boldsymbol{\rho}, t)$ is a linear transformation of the zero-mean Gaussian random process $E_S(\boldsymbol{\rho}, t)$, hence it too is a zero-mean, Gaussian random process. Thus, as in Gaussian-state analysis of transmissive ghost imaging,[4] we can employ Gaussian moment-factoring to reduce Eq. (10) to

$$\langle C(\boldsymbol{\rho}_1) \rangle = \frac{A_1 A_2 q^2 \eta^2}{L^2} \int d\tau_1 \int d\tau_2 \int d\boldsymbol{\rho}_2 \left[\langle |E_1(\boldsymbol{\rho}_1, \tau_1)|^2 \rangle \langle |E_1(\boldsymbol{\rho}_2, \tau_2)|^2 \rangle + |\langle E_1^*(\boldsymbol{\rho}_1, \tau_1) E_1(\boldsymbol{\rho}_2, \tau_2) \rangle|^2 \right] \mathcal{T}(\boldsymbol{\rho}_2)$$
$$\times h(t - \tau_1) h(t - \tau_2). \tag{11}$$

Pseudothermal ghost imaging is performed with spatially incoherent light, i.e., $\rho_0 \ll a_0$ holds in the source's Gaussian-Schell model spatial correlation. Moreover, stand-off sensing pseudothermal ghost imaging will be performed in the far field, for which $k_0 a_0 \rho_0 / 2L \ll 1$ prevails. Following Erkmen and Shapiro,[5] we then get

$$\langle E_1^*(\boldsymbol{\rho}_1, t_1) E_1(\boldsymbol{\rho}_2, t_2) \rangle = K'(\boldsymbol{\rho}_1, \boldsymbol{\rho}_2) R(t_2 - t_1), \tag{12}$$

i.e., propagation only affects the spatial coherence, which retains the Gaussian-Schell model form,

$$K'(\boldsymbol{\rho}_1, \boldsymbol{\rho}_2) = \frac{2P}{\pi a_L^2} e^{ik_0(|\boldsymbol{\rho}_2|^2 - |\boldsymbol{\rho}_1|^2)/2L} e^{-(|\boldsymbol{\rho}_1|^2 + |\boldsymbol{\rho}_2|^2)/a_L^2 - |\boldsymbol{\rho}_1 - \boldsymbol{\rho}_2|^2/2\rho_L^2}, \tag{13}$$

with $a_L = 2L/k_0\rho_0$ and $\rho_L = 2L/k_0 a_0$ being the new intensity and coherence radii, respectively.

The final ingredient we need to reduce Eq. (10) to a form in which we can easily assess the reflective ghost image's spatial resolution and image contrast is the detector's impulse response, $h(t)$. For now, let us take this to be a DC-coupled Gaussian of bandwidth Ω_B,[‡] i.e.,

$$h(t) = \frac{\Omega_B}{\sqrt{8\pi}} e^{-\Omega_B^2 t^2/8}. \tag{14}$$

Because we have assumed that the detector bandwidth is sufficient to follow the temporal behavior of the light emerging from the ground glass, we have that $\Omega_B T_0 \gg 1$. Thus we get rid of the temporal integrals and obtain

$$\langle C(\boldsymbol{\rho}_1) \rangle = \frac{A_1 A_2 q^2 \eta^2}{L^2} \left(\frac{2P}{\pi a_L^2} \right)^2 \int d\boldsymbol{\rho}_2 \left[1 + e^{-2(|\boldsymbol{\rho}_1|^2 + |\boldsymbol{\rho}_2|^2)/a_L^2} e^{-|\boldsymbol{\rho}_1 - \boldsymbol{\rho}_2|^2/\rho_L^2} \right] \mathcal{T}(\boldsymbol{\rho}_2). \tag{15}$$

When the intensity radius a_L is much larger than the target's transverse extent, so that the entire target is uniformly illuminated on average, we get our final form for the ensemble-averaged photocurrent cross correlation,

$$\langle C(\boldsymbol{\rho}_1) \rangle = \frac{A_1 A_2 q^2 \eta^2}{L^2} \left(\frac{2P}{\pi a_L^2} \right)^2 \int d\boldsymbol{\rho}_2 \left[1 + e^{-|\boldsymbol{\rho}_1 - \boldsymbol{\rho}_2|^2/\rho_L^2} \right] \mathcal{T}(\boldsymbol{\rho}_2). \tag{16}$$

Equation (16) shows that the ensemble-average photocurrent cross correlation consists of a featureless background term,

$$C_0 = \frac{A_1 A_2 q^2 \eta^2}{L^2} \left(\frac{2P}{\pi a_L^2} \right)^2 \int d\boldsymbol{\rho}_2 \, \mathcal{T}(\boldsymbol{\rho}_2), \tag{17}$$

plus the ghost-image term,

$$C_1(\boldsymbol{\rho}_1) = \frac{A_1 A_2 q^2 \eta^2}{L^2} \left(\frac{2P}{\pi a_L^2} \right)^2 \int d\boldsymbol{\rho}_2 \, \mathcal{T}(\boldsymbol{\rho}_2) e^{-|\boldsymbol{\rho}_1 - \boldsymbol{\rho}_2|^2/\rho_L^2}. \tag{18}$$

Moreover, the ghost-image term can be seen to be the target's intensity-reflection coefficient $\mathcal{T}(\boldsymbol{\rho}_2)$ convolved with a Gaussian point-spread function that limits the spatial resolution to the target-plane coherence length $\rho_L = \lambda_0 L/\pi a_0$. This is the same spatial resolution that was previously found via Gaussian-state analysis for far-field transmissive ghost-imaging with a pseudothermal source.[4] Indeed, the only difference between Eq. (18) and the corresponding result for the transmissive case is the factor A_2/L^2 that appears in the former. In transmissive ghost imaging all the light that passes through the target is collected by the bucket detector, but the quasi-Lambertian nature of the rough-surfaced target combines with the stand-off measurement by the bucket detector to introduce the solid-angle subtense factor $A_2/L^2 \ll 1$ in Eq. (18).

Turning now to the image contrast implied by Eq. (16), we will employ the contrast definition[4]

$$\mathcal{C} = \frac{\max_{\mathcal{R}}[C(\boldsymbol{\rho}_1)] - \min_{\mathcal{R}}[C(\boldsymbol{\rho}_1)]}{C_0}, \tag{19}$$

with the assumption that the target is entirely contained within a region $\mathcal{R}$ centered at the origin in transverse coordinates and having diameter that is much smaller than a_L. For simplicity, we will also assume that ρ_L is small enough to resolve all features in the target's intensity-reflection coefficient, so that

$$\int d\boldsymbol{\rho}_2 \, \mathcal{T}(\boldsymbol{\rho}_2) e^{-|\boldsymbol{\rho}_1 - \boldsymbol{\rho}_2|^2/\rho_L^2} \approx \pi \rho_L^2 \mathcal{T}(\boldsymbol{\rho}_1), \tag{20}$$

[‡]The frequency response associated with this impulse response is $H(\Omega) = \int dt \, h(t) e^{-i\Omega t} = e^{-2\Omega^2/\Omega_B^2}$

whence

$$\mathcal{C} \approx \pi \rho_L^2 / A_T, \tag{21}$$

where $A_T = \int d\boldsymbol{\rho}_2 \mathcal{T}(\boldsymbol{\rho}_2)$ is the effective area of the target. Thus $\mathcal{C} \approx 1/\text{number of on-target resolution cells}$. This image contrast coincides with what was previously derived for DC-coupled transmissive ghost imaging in far-field operation.[4]

2.3 Signal-to-Noise Ratio

The featureless background that we encountered in the preceding subsection can be eliminated by means of AC-coupling one or both of the photodetectors in the Fig. 1 setup, as has sometimes been done in pseudothermal ghost-imaging experiments.[10] Signal-to-noise ratio analysis for transmissive ghost imaging is simplified substantially by inclusion of such AC-coupled detectors,[6] so we shall take the same route here by assuming that the photodetectors' baseband frequency response include a DC block. Specifically, the detectors' frequency response is now modeled by

$$H_B(\Omega) = e^{-2\Omega^2/\Omega_B^2} - e^{-2\Omega^2/\Omega_N^2}, \tag{22}$$

where the DC-notch bandwidth, Ω_N, is much smaller than both Ω_B, the detectors' high-frequency cutoff, and $1/T_0$, the source bandwidth.[§] With this AC-coupling we have that the average photocurrent cross correlation is background free, viz., Eq. (16) becomes

$$\langle C(\boldsymbol{\rho}_1) \rangle = \frac{A_1 A_2 q^2 \eta^2}{L^2} \left(\frac{2P}{\pi a_L^2} \right)^2 \int d\boldsymbol{\rho}_2 \, e^{-|\boldsymbol{\rho}_1 - \boldsymbol{\rho}_2|^2 / \rho_L^2} \mathcal{T}(\boldsymbol{\rho}_2). \tag{23}$$

Thus it is appropriate to define the ghost image's signal-to-noise ratio (SNR) at the image point $\boldsymbol{\rho}_1$ via

$$\text{SNR} = \frac{\langle C(\boldsymbol{\rho}_1) \rangle^2}{\text{Var}[C(\boldsymbol{\rho}_1)]} = \frac{\langle C(\boldsymbol{\rho}_1) \rangle^2}{\langle C^2(\boldsymbol{\rho}_1) \rangle - \langle C(\boldsymbol{\rho}_1) \rangle^2}, \tag{24}$$

i.e, it is the ratio of the squared strength of the image component of the photocurrent cross correlation divided by the variance of that cross correlation.

Equation (23) provides an expression for the numerator in Eq. (24) and the second term in its denominator. However, to simplify our results, we shall assume that ρ_L is sufficiently small to resolve all features in $\mathcal{T}(\boldsymbol{\rho})$, reducing Eq. (23) to

$$\langle C(\boldsymbol{\rho}_1) \rangle = \frac{A_1 A_2 q^2 \eta^2}{L^2} \left(\frac{2P}{\pi a_L^2} \right)^2 \pi \rho_L^2 \mathcal{T}(\boldsymbol{\rho}_1). \tag{25}$$

This leaves us with the formidable task of evaluating

$$\langle C^2(\boldsymbol{\rho}_1) \rangle = \frac{1}{T_I^2} \int_{-T_I/2}^{T_I/2} dt \int_{-T_I/2}^{T_I/2} du \, \langle i_1(t) i_2(t) i_1(u) i_2(u) \rangle, \tag{26}$$

which requires us to determine an eighth moment of the fields and a fourth moment of the target's field-reflection coefficient. Fortunately, Gaussian-moment factoring can be applied to both of these moment evaluations, but the Fresnel-propagation kernels that cancelled out in finding the average photocurrent cross correlation do not do so here. We can simplify the analysis by using the difference coordinates $\boldsymbol{\nu} = \rho_L k_0 (\boldsymbol{\rho}' - \boldsymbol{\rho}'')/L$, where $\boldsymbol{\rho}'$ and $\boldsymbol{\rho}''$ are coordinates at the bucket detector, and defining $A_T' = \int d\boldsymbol{\rho} |\mathcal{T}(\boldsymbol{\rho})|^2$ and

$$\Gamma = \pi \int_{|\boldsymbol{\nu}| \leq 4\alpha} d\boldsymbol{\nu} \, e^{-|\boldsymbol{\nu}|^2/2} O(\boldsymbol{\nu}), \tag{27}$$

[§]Because we have assumed a narrowband pseudothermal source, $\Omega_N T_0 \ll 1$ is a more stringent condition than $\Omega_N \ll \Omega_B$.

where $O(\boldsymbol{\nu})$ is the dimensionless version of the two-circle overlap function,

$$O(\boldsymbol{\nu}) = \left[\cos^{-1}\left(\frac{|\boldsymbol{\nu}|}{4\alpha}\right) - \frac{|\boldsymbol{\nu}|}{4\alpha}\sqrt{1 - \frac{|\boldsymbol{\nu}|^2}{16\alpha^2}}\right]\frac{2}{\pi}, \tag{28}$$

with $\alpha = \sqrt{A_2/\pi a_0^2}$. Next, we assume that $A_T'/\rho_L^2 \gg 30$, which is equivalent to saying that the ghost-image consists of at least 10×10 resolution cells. Finally we assume that $A_2/\pi a_0^2 \geq 1$, which amounts to saying that the bucket detector collects light from a region whose area is at least as big as the source area. With these conditions in hand, we find that

$$\text{SNR} = \frac{\mathcal{T}^2(\boldsymbol{\rho}_1)\frac{T_I}{T_0}}{\frac{A_T'}{\sqrt{2\pi}\rho_L^2} + \mathcal{T}^2(\boldsymbol{\rho}_1)\frac{T_I}{T_0}\frac{\Gamma a_0^2}{4\pi A_2} + \frac{\mathcal{T}(\boldsymbol{\rho}_1)}{\eta\mathcal{I}}\frac{L^2}{A_2} + \frac{4\pi\rho_L^2\mathcal{T}^2(\boldsymbol{\rho}_1)}{3A_1\eta\mathcal{I}} + \frac{\mathcal{T}(\boldsymbol{\rho}_1)T_0\Omega_B\rho_L^2\sqrt{\pi}}{16\sqrt{2}A_1\eta^2\mathcal{I}^2}\frac{L^2}{A_2}}, \tag{29}$$

where $\mathcal{I} = PT_0\rho_0^2/a_0^2$ is the source brightness in photons per spatiotemporal mode.

The terms in the noise denominator of Eq (29), which originate from different combinations of field variations and shot noises, have important physical interpretations. From left to right in that denominator we have: the noise contributed by target-plane speckle from the pseudothermal illumination: the noise contributed by the speckle on the bucket detector arising from the target's surface roughness; the beat noise between the pseudothermal speckle on the CCD pixel and the bucket detector's shot noise; the beat noise between the CCD pixel's shot noise and the pseudothermal speckle on the bucket detector; and the beat noise between the shot noises on the two detectors. From here it is of interest to look at the low-brightness ($\mathcal{I} \ll 1$) and high-brightness ($\mathcal{I} \gg 1$) SNR asymptotes. These are given by

$$\text{SNR}_L = \frac{16\sqrt{2}}{\sqrt{\pi}}\frac{T_I}{T_0}\frac{A_1\eta^2\mathcal{I}^2}{\Omega_B T_0\rho_L^2}\mathcal{T}(\boldsymbol{\rho}_1)\frac{A_2}{L^2}, \tag{30}$$

and

$$\text{SNR}_H = \frac{\mathcal{T}^2(\boldsymbol{\rho}_1)\frac{T_I}{T_0}}{\frac{A_T'}{\sqrt{2\pi}\rho_L^2} + \mathcal{T}^2(\boldsymbol{\rho}_1)\frac{T_I}{T_0}\frac{\Gamma a_0^2}{4\pi A_2}}, \tag{31}$$

respectively. The low-brightness SNR is dominated by the beat noise between the detectors' shot noises. It coincides with the low-brightness SNR found for transmissive ghost imaging,[6] except for the following two differences: the reflective case has the target's average intensity-reflection coefficient, $\mathcal{T}(\boldsymbol{\rho}_1)$, appearing in lieu of transmissive target's $|T(\boldsymbol{\rho}_1)|^2$; and the reflective case includes the solid-angle scaling factor, A_2/L^2, previously encountered in our comparison of the these ghost imager's spatial resolutions.

The reflective ghost imager's high-brightness SNR asymptote is controlled by the two speckle terms from Eq (29), i.e., the speckle arising from the pseudothermal source's spatial incoherence and the speckle arising from the target's surface roughness. Neither speckle noise can be said to universally dominate the high-brightness SNR asymptote, as their relative strengths are governed by both spatial and temporal factors. We need to look at two limiting cases: when the integration time is short enough that the purely spatial term in the noise denominator dominates, and when the integration time is long enough that the other denominator term dominates. These short-time and long-time high-brightness SNR asymptotes are

$$\text{SNR}_{H,\text{ short-}T_I} = \sqrt{2\pi}\frac{T_I}{T_0}\frac{\rho_L^2}{A_T'}\mathcal{T}^2(\boldsymbol{\rho}_1), \tag{32}$$

and

$$\text{SNR}_{H,\text{ long-}T_I} = \frac{4\pi A_2}{\Gamma a_0^2}. \tag{33}$$

Here we see the short-integration-time, high-brightness SNR for reflective ghost imaging equals the high-brightness SNR for transmissive ghost imaging with $\mathcal{T}^2(\boldsymbol{\rho}_1)$ appearing instead of $|T(\boldsymbol{\rho}_1)|^4$. This agreement is to be expected,

as both of these SNRs are limited by the speckle created by the pseudothermal illumination. However, as the integration time increases, the high-brightness SNR for the reflective case saturates at the value given by Eq. (33). Here the SNR is limited by the target-induced speckle. Because we have assumed a stationary target whose field-reflection coefficient is constant, no amount of post-detector integration will reduce its speckle noise, hence SNR saturation occurs. Furthermore, this effect can be severe: for $A_2/\pi a_0^2 = 1$ we get $\text{SNR}_{H,\text{long}T_I} = 3.266$, and for $A_2/\pi a_0^2 = 2$ we find $\text{SNR}_{H,\text{long}T_I} = 5.54$. So, for realistic stand-off sensing, the SNR will be limited to single-digit values if no further measures are taken to average out the target-induced speckle.

3. COMPUTATIONAL GHOST IMAGING IN REFLECTION

Ghost imaging requires knowledge of the time-varying speckle pattern illuminating the target. Because the ground-glass diffuser in Fig. 1 randomly modulates the source field, we measure the signal field's speckle pattern with the CCD array, and exploit its correlation with the speckle pattern impinging on the target to form the ghost image. Suppose, however, that the source is subjected to a deterministic spatiotemporal modulation, through use of a spatial light modulator (SLM), in a manner that projects a time-varying but deterministic speckle pattern on the target. In this case the speckle pattern at the target can be computed from diffraction theory, and we do not need the signal arm to form a ghost image.[8] As shown in Fig. 2, we form a computational ghost image by cross correlating the computed signal-arm photocurrent,

$$\tilde{i}_1(t) = \int d\tau \, q\eta \tilde{P}_1(\tau) h(t-\tau), \tag{34}$$

with the measured photocurrent, $i_2(t)$, from the bucket detector. Here,

$$\tilde{P}_1(t) = A_1 |\tilde{E}_1(\boldsymbol{\rho}_1, t)|^2, \tag{35}$$

gives the computed photon flux for a CCD pixel located at $\boldsymbol{\rho}_1$ in terms of the computed speckle pattern $|\tilde{E}_1(\boldsymbol{\rho}_1, t)|^2$.

For comparison with the pseudothermal ghost imager, we would like to derive the spatial resolution, image contrast, and signal-to-noise ratio of its computational counterpart. To do so, we shall assume that the deterministic field pattern $\tilde{E}_1(\boldsymbol{\rho}_1, t)$ cast by the SLM in Fig 2 can be treated, for this analysis, as though it were a zero-mean, complex-valued Gaussian random process that is completely characterized by the same Gaussian-Schell model we found for the target-plane field in the pseudothermal case. With this assumption, all the derivations from Sec. 2 carry over to computational ghost imaging by simple omission of the CCD array's shot noise. Hence, the spatial resolution of the computational ghost imager is identical to that of the pseudothermal ghost imager, and, for DC-coupled operation, they have the same image contrast. Moreover, AC-coupling of the bucket detector's photocurrent or the CCD array's computed photocurrent will eliminate the featureless background term in the photocurrent cross correlation, giving the computational ghost imager the same high-contrast behavior seen earlier for AC-coupling in pseudothermal ghost imaging.

There is an interesting difference between computational and pseudothermal ghost imaging that appears when we compare their SNR formulas. As there is no longer any signal-detector shot noise, we find that the computational ghost image's SNR is given by

$$\text{SNR}_{\text{comp}} = \frac{\mathcal{T}^2(\boldsymbol{\rho}_1)\frac{T_I}{T_0}}{\frac{A_T'}{\sqrt{2\pi}\rho_L^2} + \mathcal{T}^2(\boldsymbol{\rho}_1)\frac{T_I}{T_0}\frac{\Gamma a_0^2}{4\pi A_2} + \frac{\mathcal{T}(\boldsymbol{\rho}_1)}{\eta \mathcal{I}}\frac{L^2}{A_2}}. \tag{36}$$

Comparing this formula with the pseudothermal result from Eq. (29) we see that the noise denominator for the computational ghost image's SNR contains, from left to right, terms that represent: the noise from the speckle pattern cast on the target; the noise from the speckle on the bucket detector arising from the target's surface roughness; and the beat noise between the computed speckle on the CCD pixel and the bucket detector's shot noise. It follows that the high-brightness SNR asymptote for computational ghost imaging is identical to that for
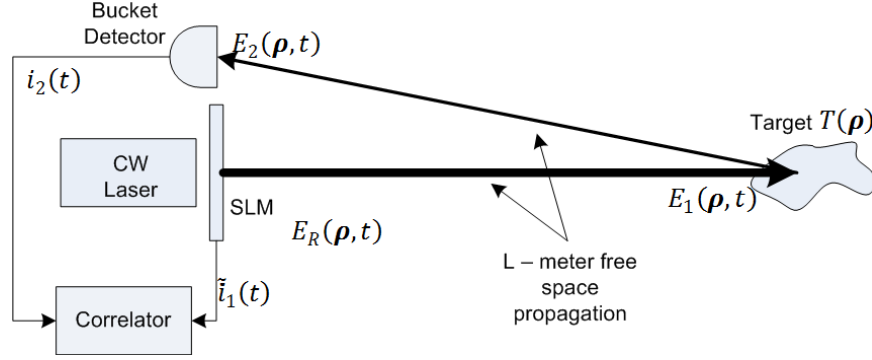
Figure 2. Setup for computational reflective ghost imaging.

pseudothermal ghost imaging. However, the computational ghost image's SNR enjoys a considerable advantage at low source brightness, viz., its low-brightness asymptote,

$$\text{SNR}_{\text{comp}, L} = \mathcal{T}(\boldsymbol{\rho}_1) \frac{T_I}{T_0} \eta \mathcal{I} \frac{A_2}{L^2}, \tag{37}$$

is significantly higher than that for the pseudothermal ghost image because it scales linearly, rather than quadratically, with source brightness.

4. COMPARISON TO A LASER RADAR SYSTEM

4.1 Theoretical Setup

The importance of ghost imaging for stand-off sensing rests on its offering some advantage over a comparable laser radar system for the same application. Here we will use the results we have developed so far to provide a preliminary comparison of ghost imaging versus laser radar as stand-off sensors. The laser radar system we shall consider is shown in Fig. 3. It is a direct-detection system in which a cw laser beam is used to produce a spatially-coherent beam at range L whose deterministic intensity pattern matches—in both photon flux and intensity radius—the average intensity pattern of the Gaussian-Schell model we employed for the ghost imager. A fraction of the laser light reflected by the target is focused by a lens that is co-located with the laser transmitter onto a CCD array. A target image is then formed by T_I-s time averaging of the output currents from each CCD pixel. The entrance pupil for the laser radar's receiving lens will be taken to coincide with the bucket detector's $\mathcal{A}_2$ active region in the ghost imager, and we will assume shot-noise limited CCD operation as was the case for the Fig. 1.[¶]

The laser radar image for the CCD pixel at location $\boldsymbol{\rho}_1$ is

$$I(\boldsymbol{\rho}_1) = \frac{1}{T_I} \int_{-T_I/2}^{T_I/2} dt \ i_3(t), \tag{38}$$

where $i_3(t)$ is the photocurrent from that pixel. This photocurrent will have the same structure as seen, for ghost imaging, in Eq (2), i.e., it will consist of a term driven by the photon flux $P_3(t)$ illuminating the pixel in question plus the shot noise from that pixel. We shall assume the DC-coupled photodetector model from Eq. (14), and we will assume the pixels are small enough that they do not limit the laser radar's spatial resolution. Once again we shall assume 1:1 imaging, although the actual system will cast a minified image on the CCD, and we shall invert the image plane coordinates so as to obtain an erect image of the target. With these assumptions

---

[¶]We recognize that most laser radar systems employ pulsed sources. We have chosen the cw case to put the laser radar on the most equal footing with the ghost imager for a baseline comparison between their spatial resolutions, image contrasts, and signal-to-noise ratios.
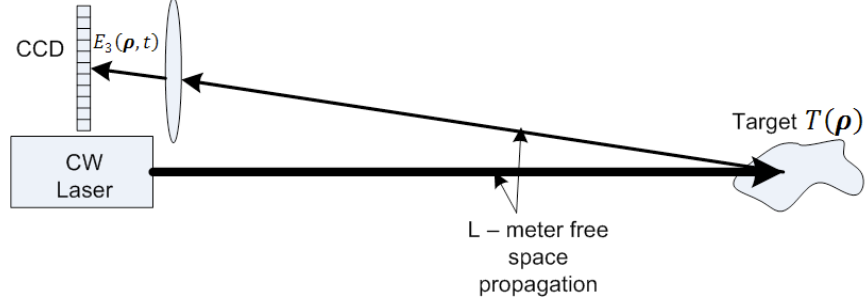
Figure 3. Setup for direct-detection laser radar.

standard Fourier-optics thin lens theory leads to the following expression for $E_3(\boldsymbol{\rho}_1, t)$, the field illuminating the CCD pixel at $\boldsymbol{\rho}_1$:

$$E_3(\boldsymbol{\rho}_1, t) = \int d\boldsymbol{\rho}\, T(\boldsymbol{\rho}) e^{ik_0|\boldsymbol{\rho}|^2/2L} \sqrt{\frac{2P}{\pi a_L^2}} e^{-|\boldsymbol{\rho}|^2/a_L^2} \frac{A_2}{\lambda_0^2 L^2} \frac{J_1(\pi D_2|\boldsymbol{\rho} - \boldsymbol{\rho}_1|/\lambda_0 L)}{\pi D_2|\boldsymbol{\rho} - \boldsymbol{\rho}_1|/2\lambda_0 L}, \tag{39}$$

where D_2 is the diameter of $\mathcal{A}_2$, J_1 is the first-order Bessel function of the first kind, and we have suppressed absolute and quadratic phase factors that do not contribute to $|E_3(\boldsymbol{\rho}_1, t)|^2$. The photon flux for the pixel at $\boldsymbol{\rho}_1$ is thus $P_3(t) = A_1|E_3(\boldsymbol{\rho}_1, t)|^2$, and the photocurrent $i_3(t)$ is

$$i_3(t) = q\eta P_3(t) + \Delta i_3(t), \tag{40}$$

where the second term is the shot noise. In keeping with what we did for ghost imaging, we shall assume that the target is uniformly illuminated by the laser radar, so that we can use $e^{-|\boldsymbol{\rho}|^2/a_L^2} \approx 1$ in Eq. (39).

4.2 Spatial Resolution and Image Contrast

To derive the laser radar's spatial resolution and image contrast, we once again look at the ensemble-averaged image. Averaging Eq. (38) over the target's surface roughness and the detector's shot noise we find

$$\langle I(\boldsymbol{\rho}_1) \rangle = \frac{q\eta A_1 A_2^2}{\lambda_0^2 L^4} \frac{2P}{\pi a_L^2} \int d\boldsymbol{\rho}\, T(\rho) \left(\frac{J_1(\pi D_2|\boldsymbol{\rho} - \boldsymbol{\rho}_1|/\lambda_0 L)}{\pi D_2|\boldsymbol{\rho} - \boldsymbol{\rho}_1|/2\lambda_0 L} \right)^2, \tag{41}$$

which shows that the target image is proportional to the target's intensity-reflection coefficient convolved with the familiar Airy disk point-spread function for incoherent imaging. Hence our laser radar has a spatial resolution given by $1.22\lambda_0 L/D_2$. In our ghost imaging setup, with $D_2 = 2a_0$, the spatial resolution is given by $\rho_L = \lambda_0 L/\pi a_0 = 2\lambda_0 L/\pi D_2$, which is comparable to that of the laser radar. Equation (41) also shows that our direct-detection laser radar's image is not embedded in a featureless background, making its image contrast superior to that of DC-coupled pseudothermal ghost imaging but equivalent to that of the AC-coupled version.

4.3 Signal-to-Noise Ratio

We define the laser radar's SNR by

$$\text{SNR} = \frac{\langle I(\boldsymbol{\rho}_1) \rangle^2}{\text{Var}[I(\boldsymbol{\rho}_1)]} = \frac{\langle I(\boldsymbol{\rho}_1) \rangle^2}{\langle I^2(\boldsymbol{\rho}_1) \rangle - \langle I(\boldsymbol{\rho}_1) \rangle^2}, \tag{42}$$

to enable a direct comparison with the ghost imaging SNR from Eq (24). We will assume that the Airy disk point-spread-function resolves all significant features in the target's intensity-reflection coefficient, yielding

$$\langle I(\boldsymbol{\rho}_1) \rangle = \frac{q\eta A_1 A_2}{L^2} \frac{2P}{\pi a_L^2} \mathcal{T}(\boldsymbol{\rho}_1). \tag{43}$$

The variance calculation we need is much simpler than what we performed for ghost imaging. Making use of the iterated-expectation formula,

$$
\begin{aligned}
\mathrm{Var}[I(\boldsymbol{\rho}_1)] &= E_{\{P_3(t):-T_I/2\leq t\leq T_I/2\}}[\mathrm{Var}(\,I(\boldsymbol{\rho}_1))\mid\{P_3(t):-T_I/2\leq t\leq T_I/2\}\,)] \\
&\quad + \mathrm{Var}_{\{P_3(t):-T_I/2\leq t\leq T_I/2\}}[E(\,I(\boldsymbol{\rho}_1)\mid\{P_3(t):-T_I/2\leq t\leq T_I/2\}\,)],
\end{aligned}
\tag{44}
$$

we can easily evaluate the noise denominator in Eq. (42). The first term on the right in Eq. (44) is due to the target-induced speckle, and is given by $\langle I(\boldsymbol{\rho}_1)\rangle^2$, and the second term on the right in that equation is due to the shot noise, and is given by $q\langle I(\boldsymbol{\rho}_1)\rangle/T_I$. This leaves us with

$$
\mathrm{SNR} = \frac{\mathcal{T}(\boldsymbol{\rho}_1)}{\mathcal{T}(\boldsymbol{\rho}_1) + \dfrac{L^2}{\eta A_1 A_2}\dfrac{\pi a_L^2}{2PT_I}}.
\tag{45}
$$

From this SNR expression we immediately see that when the combination of source brightness and integration time is sufficiently high, the laser radar's SNR saturates at a maximum value of unity, limited by the target-induced speckle. With the small CCD pixels we have assumed, ghost imaging still experiences a spatial averaging of the target speckle on the bucket detector, whereas no such effect is available for the laser radar system. Thus when both systems have target-speckle limited SNRs, the laser radar's performance is inferior to that of the ghost imager. However, outside of this limiting scenario, the relationship between the two system's SNRs is more complicated, as we will now show.

To compare the stand-off sensing SNRs for ghost imaging and direct-detection laser radar in more detail, consider the plots shown in Figs. 4(a) and 4(b). Both figures assume $\lambda_0 = 1.5\,\mu\mathrm{m}$ operation for ghost imaging and laser radar, with their transmitters having the same photon flux. For ghost imaging we assume the source parameters are $a_0 = 1\,\mathrm{cm}$ and $\rho_0 = 0.15/\pi\,\mathrm{mm}$. The target is assumed to be at $L = 1\,\mathrm{km}$ range, with effective area $A'_T = 100\,\mathrm{m}^2$. Thus $a_L = \lambda_0 L/\pi\rho_0 = 10\,\mathrm{m}$ implies that the target illumination is nearly uniform on average, with speckle-limited spatial resolution given by $\rho_L = \lambda_0 L/\pi a_0 = 0.15/\pi\,\mathrm{m}$. The CCD array's pixel area will be taken to satisfy $A_1 = 0.1\rho_L^2$, and the bucket detector's area will be set to $A_2 = \pi a_0^2$. Both detectors will have $\eta = 0.9$ quantum efficiency with bandwidths obeying $\Omega_B T_0 = 100$. The laser radar's transmitter will produce a spatially-coherent Gaussian intensity pattern on the target with the same a_L value, and its CCD array will be identical to that of the ghost imager. Figure 4(a) plots the SNRs for pseudothermal ghost imaging, computational ghost imaging, and direct-detection laser radar operation versus the normalized integration time, T_I/T_0, when $\mathcal{T}(\boldsymbol{\rho}_1) = 1$ and the ghost-imaging transmitter's source brightness is $\mathcal{I} = 10^9$ photons/mode. This figure shows a slight SNR advantage for laser radar operation when $T_I/T_0 < 10^4$, with the ghost imagers offering higher SNRs when all three systems reach their target-speckle limits. Figure 4(b) plots the three systems' SNRs versus the ghost imager's source brightness assuming $\mathcal{T}(\boldsymbol{\rho}_1) = 1$ and $T_I/T_0 = 10^7$. Here we see that computational ghost imaging provides the best performance, while laser radar operation is the worst performer except for $\mathcal{I} \sim 10^{-2}$. Pseudothermal ghost imaging is outperformed by computational operation until both systems' SNRs reach their common target-speckle limit.

5. CONCLUSIONS

We have derived expressions for the spatial resolutions, image contrasts, and signal-to-noise ratios of pseudothermal and computational reflective ghost-imaging. The spatial resolutions of the pseudothermal and computational cases coincide with each other and with that for pseudothermal ghost imaging in transmission. The image contrast for the pseudothermal case in DC-coupled operation matches that for the similar setup used in transmission, while AC-coupled pseudothermal ghost imaging and computational ghost imaging have the same high contrast as AC-coupled ghost imaging in transmission. Thus the principal performance difference between ghost imaging in reflection and transmission lies in the SNR behavior, with the former suffering from the ill-effects of target-induce speckle that are absent in the latter. Moreover, because of the absence of signal-light shot noise, computational ghost imaging in reflection can have an appreciably higher SNR than its pseudothermal counterpart. We then used our results to develop the first rigorous performance comparison for stand-off sensing using ghost imaging versus stand-off sensing using a direct-detection laser radar. It turned out that ghost imaging and laser radar
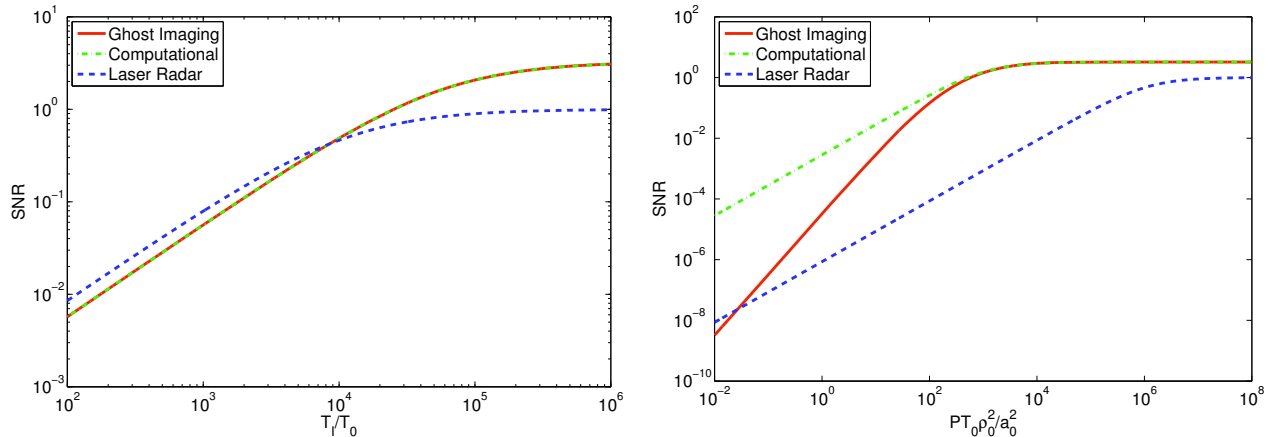
(a) Signal-to-noise ratios versus normalized integration time, T_I/T_0, for high ghost-imaging source brightness $\mathcal{I} = PT_0\rho_0^2/a_0^2 = 10^9$.

(b) Signal-to-noise ratios versus ghost-imaging source brightness, $\mathcal{I} = PT_0\rho_0^2/a_0^2$, for long integration-time operation $T_I/T_0 = 10^7$.

Figure 4. Signal-to-noise ratio comparison between pseudothermal ghost imaging, computational ghost imaging, and laser radar operation. The parameter values assumed are given in the text.

offer nearly equivalent spatial resolutions, but there were differences in their SNR behaviors, with the pseudothermal ghost imager offering an SNR advantage when both systems reached their target-speckle limits, and the computational ghost imager outperforming the laser radar at low source-brightness.

There are still several techniques that could improve ghost imaging for stand-off sensing which we have yet to incorporate into our performance analysis. An array of bucket detectors could provide additional spatial averaging of the target-induced speckle. Multiple-wavelength operation could be used to provide spectral averaging of the target-induced speckle. Both such techniques would then increase the saturation SNR in both pseudothermal and computational ghost imaging. Compressed sensing has been shown, empirically, to reduce the time needed to achieve a desired subjective quality in transmissive ghost imaging,[11] but its applicability to the reflective case and especially the SNR analysis for that case are open questions.

ACKNOWLEDGMENTS

REFERENCES

[1] A. Valencia, G. Scarcelli, M. D'Angelo, and Y. Shih, "Two-photon imaging with thermal light," Phys. Rev. Lett. **94**, 063601 (2005).

[2] F. Ferri, D. Magatti, A. Gatti, M. Bache, E. Brambilla, and L. A. Lugiato, "High-resolution ghost image and ghost diffraction experiments with thermal light," Phys. Rev. Lett. **94**, 183602 (2005).

[3] T. B. Pittman, Y. H. Shih, D. V. Strekalov, and A. V. Sergienko, "Optical imaging by means of two-photon quantum entanglement," Phys. Rev. A **52**, R3429 (1995).

[4] B. I. Erkmen and J. H. Shapiro, "Unified theory of ghost imaging with Gaussian-state light," Phys. Rev. A **77**, 043809 (2008).

[5] B. I. Erkmen and J. H. Shapiro, "Ghost imaging: from quantum to classical to computational," to appear in Adv. in Opt. and Photonics.

[6] B. I. Erkmen and J. H. Shapiro, "Signal-to-noise ratio of Gaussian-state ghost imaging," Phys. Rev. A **79**, 023833 (2009).

[7] R. Meyers, K. S. Deacon, and Y. Shih,, "Ghost-imaging experiment by measuring reflected photons," Phys. Rev. A **77**, 041801(R) (2008).

[8] J. H. Shapiro, "Computational ghost imaging," Phys. Rev. A **78**, 061802(R) (2008).

[9] J. H. Shapiro, B. A. Capron, and R. C. Harney, "Imaging and Target Detection with a Heterodyne-Reception Optical Radar," Appl. Opt., **20**, 3292–3313 (1981).

[10] G. Scarcelli, V. Berardi, and Y. Shih, "Can two-photon correlation of chaotic light be considered as correlation of intensity fluctuations?," Phys. Rev. Lett. **96**, 063602 (2006).

[11] O. Katz, Y. Bromberg, and Y. Silberberg, "Compressive ghost imaging," Appl. Phys. Lett. **95**, 113110 (2009).